

Accelerated Data-Driven Discovery and Screening of Two-Dimensional Magnets Using Graph Neural Networks

Ahmed Elrashidy,^{*,†} James Della-Giustina,[‡] and Jia-An Yan^{*,†}

[†]*Department of Physics, Astronomy, and Geosciences, Towson University, 8000 York, Towson, MD 21252, USA*

[‡]*Department of Mathematics, Towson University, 8000 York, Towson, MD 21252, USA*

E-mail: aalras2@students.towson.edu; jyan@towson.edu

Abstract

In this study, we employ Graph Neural Networks (GNNs) to accelerate the discovery of novel 2D magnetic materials which have transformative potential in spintronics applications. Using data from the Materials Project database and the Computational 2D materials database (C2DB), we train three GNN architectures on a dataset of 1190 magnetic monolayers with energy above the convex hull (E_{hull}) less than 0.3 eV/atom. Our Crystal Diffusion Variational Auto Encoder (CDVAE) generates 11,100 candidate crystals. Subsequent training on two Atomistic Line Graph Neural Networks (ALIGNN) achieves a 93% accuracy in predicting magnetic monolayers and a mean average error of 0.039 eV/atom for E_{hull} predictions. After narrowing down candidates based on magnetic likelihood and predicted energy, constraining the atom count in the monolayers to five or fewer, and performing dimensionality checks, we identify 190 candidates. These are validated using Density-Functional Theory (DFT) to confirm their magnetic and energetic favorability resulting in 167 magnetic monolayers with

$E_{\text{hull}} < 0.3$ eV/atom and a total magnetization of $\geq 0.5\mu_B$. Our methodology offers a way to accelerate exploring and predicting potential 2D magnetic materials, contributing to the ongoing computational and experimental efforts aimed at the discovery of new 2D magnets.

Introduction

Data-driven approaches have recently had a significant impact on discovering novel materials. Many methodologies in data-driven studies of materials utilize high-throughput DFT calculations, leading to the development of multiple databases of materials in one, two, and three dimensions. Prominent examples are the Materials Project (MP) Database,¹ the Joint Automated Repository for Various Integrated Simulations (JARVIS),² the Open Quantum Materials Database (OQMD),^{3,4} the Computational 2D Materials Database (C2DB),^{5,6} and the Computational 1D Materials Database (C1DB),⁷ among others. More recently, the fusion of DFT and Machine Learning (ML) techniques has become an invaluable tool for discovering new materials and understanding the properties of existing ones. Specifically, the introduction of ML approaches has offset some need for the expensive computational resources that DFT calculations often demand.⁸ One notable example of the efficiency of this hybrid approach is the experimental realization of new ultra-incompressible materials guided through a combination of DFT calculations and Bayesian Optimization.⁹ This approach has also been expanded to utilize a stacked model that combines multiple ML models coupled with high-throughput DFT to discover Fe-based bimetallic chalcogenides.¹⁰

High-throughput methods and ML models are also making progress in discovering and studying 2D materials. A combination of ML models and DFT calculations was used to explore the structural and thermodynamic stability of 2D materials, in addition to screening functional 2D materials for energy conversion and storage.¹¹⁻¹³ Moreover, a symmetry-based approach has been devised to screen for all thermodynamically stable combinations of binary and ternary 2D materials, and high-throughput DFT calculations were utilized in discovering

2D superconductors.^{14,15}

Historically, the realization of a 2D magnet has been deemed infeasible due to the Mermin-Wagner theorem unless a magnetic anisotropy is present in the system.¹⁶ The first indication of the existence of intrinsic 2D magnetism down to the monolayer limit was demonstrated through the discovery of antiferromagnetic (AFM) order in FePS₃.¹⁷ Following discoveries of ferromagnetic (FM) order in monolayer CrI₃,¹⁸ Cr₂Ge₂Te₆,¹⁹ Fe₃GeTe₂,²⁰ CrBr₃,²¹ and other materials have attracted much interest in this class of 2D materials.

The discovery of new 2D magnets has become a very active field of research due to its potential in developing the next generation of nano-electronic devices encompassing spintronics applications.²² In fact, several experimental observations of room-temperature magnetism could mean that practical applications that capitalize on this class of materials may not be too far from becoming a reality.^{23–28} Nonetheless, 2D magnets are mostly not air-stable which presents a challenge for adoption in potential applications.²⁹ Another important long-standing challenge is the realization of semiconducting magnets with critical temperatures above room temperature.³⁰ Additionally, many 2D magnets exhibit interesting quantum phenomena such as superconductivity,³¹ spin liquid states,^{32,33} and topological phases.^{34–37} Consequently, this class of materials presents itself as a playground for quantum phenomena and strongly correlated effects in addition to its numerous potential applications. As a result, many studies have been devoted to high-throughput and ML investigations to discover new 2D magnets.

One of the notable successes of these studies is pointing out that Cr₃Te₄ is a promising candidate for two-dimensional magnetism.³⁸ This material has been recently experimentally synthesized and verified to be a layer-dependent ferromagnet.³⁹ Additionally, high-throughput calculations have been utilized to screen for 2D magnetic materials based on experimental databases,⁴⁰ predict the ground state of collinear magnetic order,⁴¹ and search for magnetic topological 2D materials.⁴² Other studies have also focused on the role of magnetic anisotropy in 2D magnets.^{43–45}

Also, a semi-supervised ML approach was adopted to identify thermodynamically stable 2D magnets for spintronics applications.⁴⁶ Moreover, the investigation of 2D magnets by means of atomic substitution has been carried out for compounds of the forms $A_2B_2Te_6$ and $A^iA^{ii}B_4X_8$ using DFT and ML.^{47,48} ML approaches such as XGBoost have also proven to be effective in gaining a deeper physical understanding of the magnetic ordering of 2D magnets.^{49,50}

Despite the success of many high-throughput and ML techniques in predicting material properties and even discovering new ones, they are often limited in how they represent materials. This is due to the fact that crystalline materials often do not naturally lend themselves to traditional ML structures like vectors and matrices. To overcome this challenge, Graph Neural Networks (GNNs) emerge as a promising solution. Differing from traditional feed-forward multi-layer perceptron neural networks, GNNs excel in processing graph-structured input.⁵¹ Through message-passing mechanisms, GNNs can iteratively update node representations based on information from neighboring nodes and edges. This capability makes them particularly apt for material property exploration and inverse design.⁵²

Herein, we have generated new 2D magnets by using Crystal Diffusion Variational Autoencoder (CDVAE), a generative model designed for generating stable materials by learning from the data distribution of known materials.⁵³ Additionally, we also employ the Atomistic Line Graph Neural Network (ALIGNN)⁵⁴ and the Materials Graph with 3-body Interactions neural Network (M3GNet).⁵⁵

The advantage of using diffusion models,^{56,57} in comparison to elemental substitution, is that it streamlines the material generation process. These models eliminate the need to wade through countless potential stoichiometries and symmetries, adopting a data-driven approach instead. Additionally, graph-based diffusion models have shown great promise in tasks like designing inorganic crystals,⁵⁸ generating 1D and 2D materials,^{59,60} producing potential superconducting materials,⁶¹ and curating stable spintronic materials.⁶²

In this work, GNNs were utilized in conjunction with high-throughput DFT calculations

to methodically develop an accelerated data-driven approach for 2D magnets discovery; this is achieved through a four-fold process. First, magnetic monolayers are generated by a CDVAE model. Then, the monolayers are screened through ALIGNN models in addition to charge neutrality, electronegativity, number of atoms, and dimensionality checks. Next, a symmetry-constrained relaxation is then performed using M3GNET IAP. Finally, further DFT relaxations and self-consistent calculations are performed to assess the magnetic properties and the thermodynamic stability of the screened monolayers.

Computational Methods

CDVAE

CDVAE generates new materials by learning from the available crystalline structures in the training data. The model does not directly use pre-defined chemical formulas; instead, it learns to generate crystals that are likely to be stable by identifying energy minimums and bonding preferences between different types of atoms from the data. Hence, the compositions, ratios of elements in the generated materials, and their chemical and physical properties are indirectly derived from the training data. Additionally, it incorporates stability through a noise conditional score network as the decoder of the Variational Autoencoder (VAE).⁶³ This decoder utilizes a harmonic force field to estimate the forces on atoms when their coordinates deviate from the equilibrium positions, thereby providing an important physical inductive bias for generating stable materials. CDVAE encodes permutation, translation, rotation, and periodic invariances through SE(3) equivariant GNNs adapted with periodicity.⁶⁴ This allows CDVAE to generate valid, diverse, and realistic materials, in addition to its ability to optimize physical and chemical properties in latent space.

We utilized a CDVAE model to generate magnetic monolayers, training it on the available data of magnetic monolayers from C2DB. The database consists of more than 15,000 monolayers with a multitude of properties calculated through DFT. From C2DB, we curated

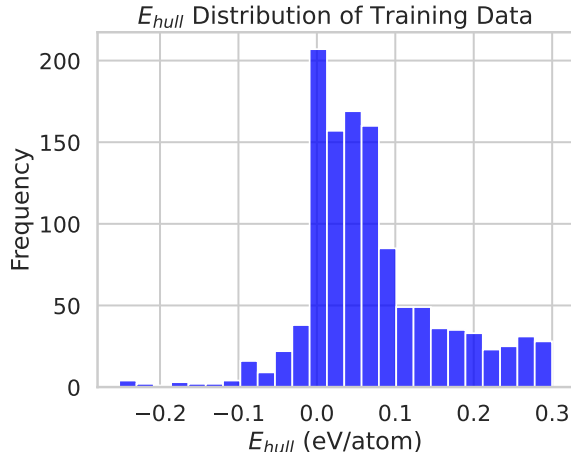


Figure 1: Distribution of E_{hull} of the 1190 training examples. The negative energies relative to the convex hull are due to monolayers that also exist in competing bulk phases with formation energies calculated using DFT+U which can lead to an overestimation of the formation energies.⁵

a dataset of 1190 monolayers by filtering only magnetic monolayers with E_{hull} less than 0.3 eV/atom. The dataset was partitioned using an 80-10-10 split, allocating 80% for training, 10% for validation, and 10% for testing. It should be emphasized that the E_{hull} cutoff value applied in this context serves not as a stability criterion, but simply as a threshold for selecting training data. This value of 0.3 eV/atom was chosen to be consistent with previous work that employed CDVAE to incorporate new entries to C2DB.⁵⁹ The distribution of the energy relative to the convex hull of the training set is shown in Figure 1.

ALIGNN

This model leverages both the atomic graph structure of the material and its corresponding line graph, which is derived from the original graph by transforming each edge into a vertex. The set of edges in the line graph is then constructed based on whether two edges shared a mutual vertex in the original graph; if so, they now share an edge in the line graph. By associating edges with the interatomic distances and vertices with the elemental properties of each atom in the original graph, alongside correlating edges with bond angles and vertices with interatomic bonds in the line graph, ALIGNN is able to capture an extensively higher

degree of information. This is achieved by sequentially performing message passing on each graph and facilitating information propagation between the two.

We trained two ALIGNN architectures using a dataset of 154,718 materials from the materials project (MP) database and an 80-10-10 split for training. The first model is a regression model to predict the E_{hull} of the entries, and the second is a classification model to predict magnetism.

M3GNET Relaxation

M3GNet is a graph neural network architecture designed to be a universal (interatomic potential) IAP for materials. It is trained on a large dataset of energies, forces, and stresses from structural relaxations performed by the Materials Project, and is capable of predicting the properties of individual atoms as well as the overall crystal structure. M3GNet uses a three-body interaction model and is able to capture long-range interactions without the need to increase the cut-off radius for bond construction. The architecture represents the elemental information for each atom as a learnable embedding vector, making it readily extendable to multicomponent chemistries.

Force Field methods have been suggested as pre-structure-optimizers before performing DFT calculations.⁶⁵ By utilizing the default pre-trained M3GNet IAP, we conducted a symmetry-constrained relaxation of the cell shape, which is achieved by applying tensile and compressive strains within the plane of the monolayers. This allows us to approach the neighborhood of the potential energy surface (PES) minima at a fraction of the cost of DFT before performing full relaxations.

DFT Calculations

For the DFT calculations, we employed the projected augmented wave (PAW) method as implemented in the Vienna *ab initio* Simulation Package (VASP).^{66,67} We chose the Perdew-Burke-Ernzerhof (PBE)⁶⁸ formulation for the generalized-gradient exchange-correlation func-

tional (GGA). The Brillouin zone underwent sampling using a $9 \times 9 \times 1$ k -point grid mesh⁶⁹ with a 600 eV plane wave cutoff energy. This mesh size was chosen so that after M3GNET relaxations, the k -point density for the smallest lattice vector in the considered materials is 4 points/Å⁻¹.

Limiting our considerations to the ferromagnetic states, initial magnetic moments were assigned to the atoms for collinear magnetic calculations without spin-orbit coupling (SOC). Transition metal elements were initialized with a magnetic moment of $6\mu_B$, while all other elements were initialized to a value of $0.5\mu_B$. This intentional overestimation aims to facilitate convergence and relaxation into the accurate ferromagnetic ground state.

Each structure was fully relaxed until the Hellmann-Feynman forces on every atom were less than 2×10^{-2} eV/Å, and the energy convergence criterion reached 10^{-6} eV. For self-consistent evaluations, a more stringent energy convergence criterion of 10^{-7} eV was applied.

It is worth noting that this approach does not consider AFM order and therefore could miss energetically favorable AFM phases, if present. As this work is concerned with developing an approach for accelerating 2D magnet discovery, considering AFM states that typically require increasing the size of the unit cell goes beyond our scope. Additionally, we have used PBE functionals throughout with no inclusion of a Hubbard-U correction in order to be consistent with the computational methodology of C2DB; this also allows for more consistent energetic favorability analysis. Nonetheless, many magnetic 2D materials exhibit strongly correlated effects and are better suited for more advanced methods that account for correlation in the outer electronic shells such as DFT+U,^{70,71} dynamical mean field theory (DMFT),⁷² and Quantum Monte Carlo.⁷³ These methods have proven to be more accurate in describing materials manifesting strong correlation effects.⁷⁴⁻⁷⁸

Results & Discussion

Generating 2D Magnets

In C2DB, the material properties of the greatest importance for our goal are the magnetic and thermodynamic ones. Specifically, we are interested in the energy above the convex hull (E_{hull}). The energy of the convex hull is derived from the Gibbs free energy at 0 K temperature and 0 atm pressure by constructing the convex hull set of the normalized formation energy with respect to the number of atoms. The energy above hull calculation provides an additional advantage over using the formation energy per atom (E_f). This advantage stems from E_{hull} assessing the energetic favorability of compounds relative to other competing phases in terms of their formation energies. Therefore, a compound’s stability is inversely proportional to its energy above the convex hull; the less stable it is, the higher its E_{hull} . In many data-driven approaches to generating materials, E_{hull} has become a standard measure to assess the thermodynamic stability of the generated materials.^{14,59–62,79–81}

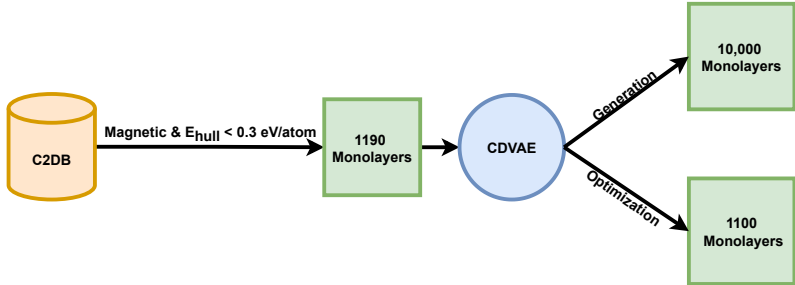


Figure 2: Outline of training CDVAE to generate 11,100 candidate monolayers for further screening.

We trained the CDVAE model to perform two tasks, generating monolayers both with and without optimization for the energy above the convex hull in latent space. The model yielded 11,100 candidate monolayers, which were subsequently screened. This process to generate these monolayers is depicted in Figure 2. For reference, the distribution of the top-generated stoichiometries by CDVAE is shown in Figure 3.

The larger portion of the materials were generated without optimization of the E_{hull} in

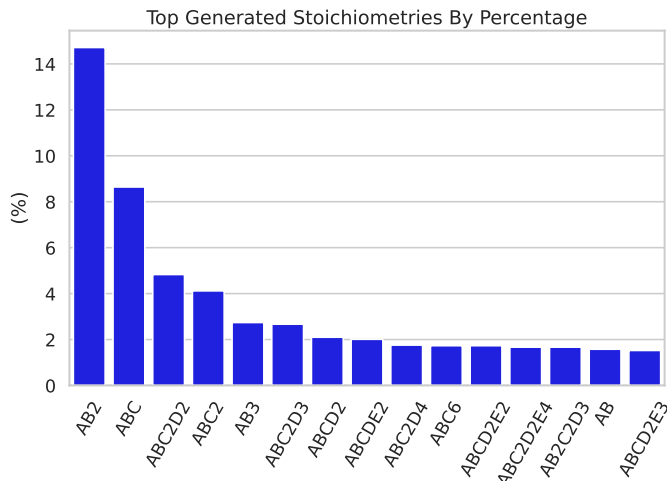


Figure 3: The distribution of stoichiometries generated by CDVAE.

the latent space. This was done to increase the number of candidates since the training dataset was filtered to only contain materials within proximity to E_{hull} .

Training ALIGNN Discriminator Models

While DFT remains the gold standard in determining the properties of 2D materials, including thermal stability and magnetic properties, performing thousands of DFT calculations requires a considerable amount of time and computational power.

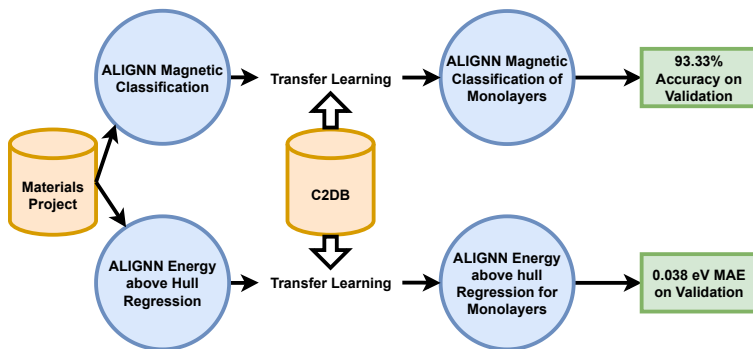


Figure 4: Outline of training CDVAE to generate 11,100 candidate monolayers for further screening.

This becomes a crucial factor when considering that many of the generated monolayers may not be magnetic or thermodynamically stable. Hence, we utilize the ALIGNN models

to filter candidates by their magnetic probability and thermal stability before running DFT calculations. The overall outline of how the ALIGNN models are utilized and the results of training are illustrated in Figure 4.

The regression model predicts E_{hull} and achieves an MAE (Mean Average Error) of 0.028 eV/atom. We then employ transfer learning and further train the model on the monolayers in C2DB to predict the energy above the convex hull and obtain an MAE of 0.039 eV/atom. The second model is utilized to classify whether a material is magnetic, which has previously been accomplished in ALIGNN performance benchmarks by specifying a cutoff value of $0.05 \mu_B$ for the total magnetic moment.⁵⁴ Using this strategy, the model attains an accuracy of 87.30% on the test dataset, likely due to the fact that this approach effectively classifies the data into ferromagnets or non-ferromagnets. Moreover, within the same material, structural deformations through strain may be associated with a change in the magnetic order.⁸²⁻⁸⁴ Fortunately, the Materials Project API provides a classification of whether a material is magnetic by considering multiple states of magnetism including ferromagnetism, antiferromagnetism, and other magnetic phases. By training the model using this classification label instead of using a cutoff value for the magnetic moment, the model accuracy improves and reaches 93.33%. Again, we apply transfer learning to train the model on classifying the monolayers in C2DB into magnetic or non-magnetic, reaching an accuracy of 93.33% on C2DB data. The performance of both the classification and regression models with and without the use of transfer learning is compared in Table 1. An early stopping condition was employed, set to activate after 15 epochs without performance improvement on the validation data. As evidenced by Table 1, models utilizing transfer learning met this condition more quickly, but interestingly did not improve the accuracy score. Additionally, the E_{hull} regression model achieves a better performance in fewer epochs.

To demonstrate the model’s robust performance in classifying magnetic materials across different symmetries, we present the model’s accuracy among the space groups in the testing data in Figure 5. As depicted by the Figure, the model accuracy is high across the majority

Table 1: The effect of transfer learning on performance on the test dataset and the speed of training.

	Magnetic Classification		E_{hull} Regression	
	Training Epochs	Accuracy	Training Epochs	MAE
With Transfer Learning	18	93.33	159	0.044
Without Transfer Learning	32	93.33	169	0.039

of the space groups in the test data.

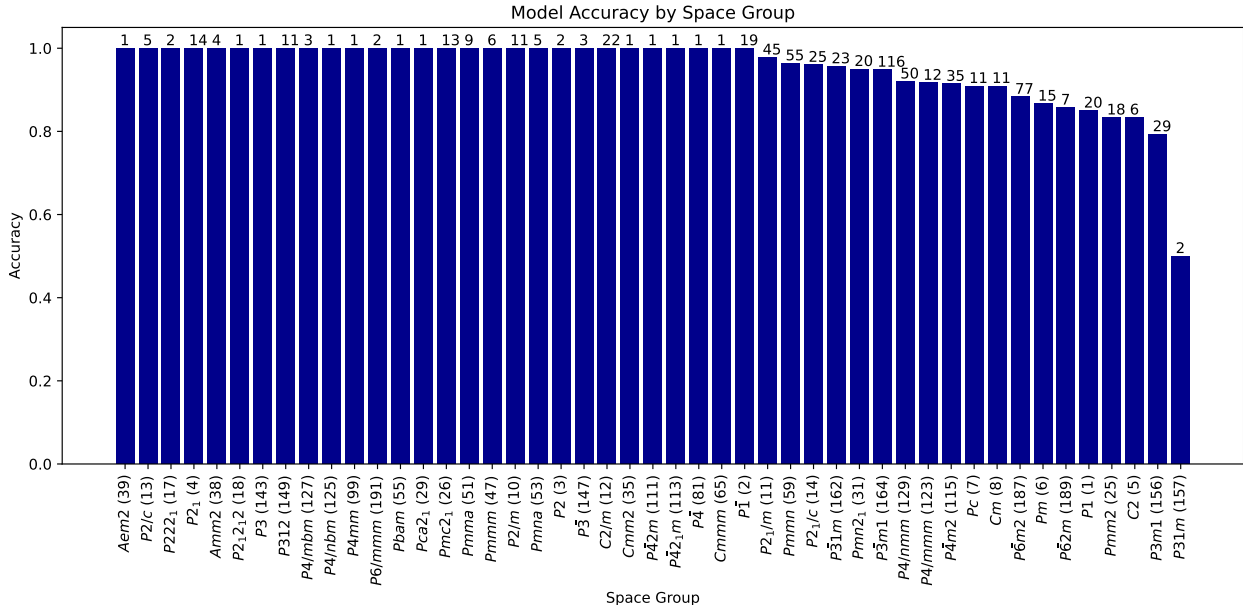


Figure 5: Model accuracy across different space groups in the test data; the number of test data points from each group is indicated on each bin.

Lattice Relaxation Through M3GNET IAP

The M3GNet IAP is a graph neural network-based approach using interatomic potentials that predicts the energies, forces, and stresses of a material.⁵⁵ To find the energetic minima, we use this model to relax the crystal shape by applying in-plane strain on the lattice. Then, the predicted energies are fitted to the volumes using the stabilized jellium equation of state provided through the atomic simulation environment (ASE).^{85,86} A visualization of the fitting process, as strain is exerted on a monolayer of Au₃Br₂SSe from C2DB (ID = 4605), is presented in Figure 6.

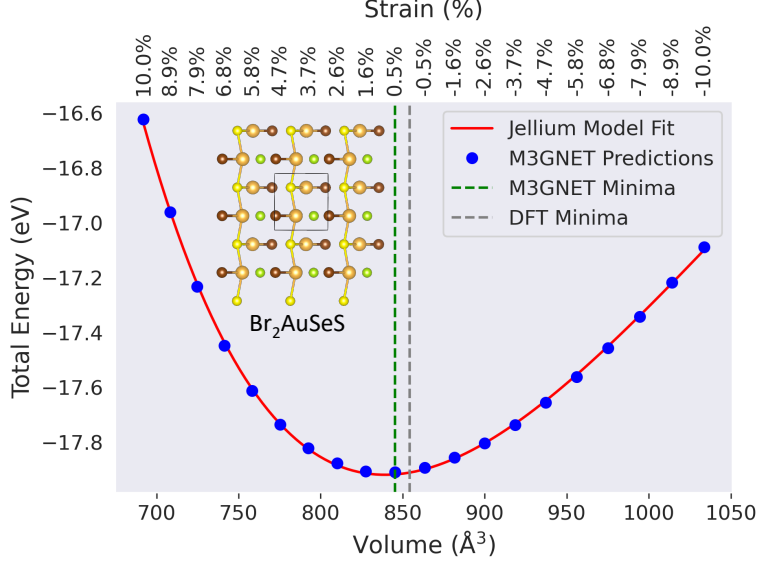


Figure 6: Symmetry-constrained relaxation by applying strain fitted to the jellium model. The energetic minima obtained using DFT and M3GNET are indicated in the plot.

To evaluate the efficacy of this model at performing symmetry-constrained relaxation, we employed the 2-norm difference between the symmetry-constrained IAP relaxation and DFT relaxed lattice vector matrices. For a given material, this is computed as $\|\mathbf{A}_{\text{IAP}} - \mathbf{A}_{\text{DFT}}\|_2$, where \mathbf{A}_{IAP} and \mathbf{A}_{DFT} are the respective lattice vector matrices. For a given set of materials, the average 2-norm difference is given by $\bar{D} = \frac{1}{N} \sum_{i=1}^N \|\mathbf{A}_{\text{IAP},i} - \mathbf{A}_{\text{DFT},i}\|_2$, where N is the total number of materials. This average \bar{D} provides a statistical measure of the IAP method’s accuracy in reproducing DFT-computed lattice parameters across a variety of materials. By computing the average 2-norm difference across all entries in C2DB, we obtained a value of $\bar{D} = 0.19 \text{ \AA}$. This result demonstrates that, through the utilization of machine learning, M3GNET IAPs are capable of achieving near DFT performance levels at a significantly reduced computational cost. For comparison, the default pre-trained atomistic line graph neural network-based force fields (ALIGNN-FF) model achieves $\bar{D} = 0.47 \text{ \AA}$. The result of the symmetry-constrained relaxation fit using ALIGNN-FF is shown in the supplementary in Figure S2.

Screening and DFT calculations

Now that all the necessary components for generating, screening, and symmetry relaxation have been developed, we integrate them into a single pipeline, shown in Figure 7.

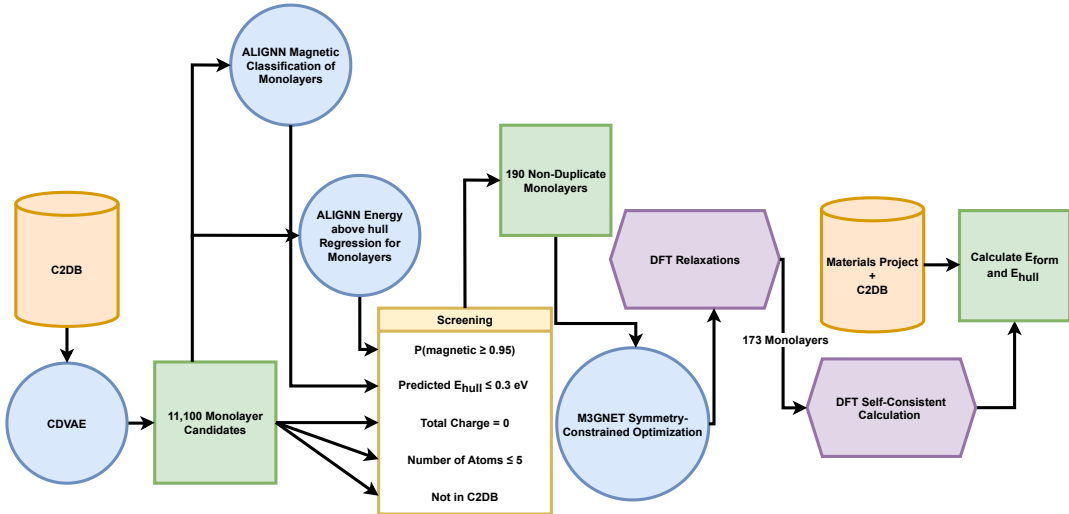


Figure 7: The full data pipeline of material generation, screening, and DFT calculations.

After the monolayer candidates have been generated by CDVAE, they are passed through a screening step. The trained ALIGNN discriminator models are then used to make predictions on the generated monolayers. We only keep monolayers where the classification model outputs a 95% probability of being magnetic and the regression model predicts the value of $E_{\text{hull}} \leq 0.3$ eV/atom. We also check for charge neutrality and run electronegativity tests as implemented in the Semiconducting Materials from Analogy and Chemical Theory (SMACT) Python library.⁸⁷

Additionally, by constraining the number of atoms in the crystal to 5 or less, we further refined the candidate pool to an order of hundreds. This value was chosen because it loosely aligns with the 25-percentile value of the number of atoms in the magnetic monolayers in C2DB, shown in Figure S1. Using a smaller number of atoms allows us to perform less computationally expensive calculations, given that DFT methods typically scale as $\mathcal{O}(N^3)$ where N is the number of atoms.⁸⁸ Duplicate materials were removed by comparing the stoichiometries to the entries available in C2DB. Finally, we implement a dimensionality check

step based on covalently bonded clusters to determine the dimensions of connected subunits in a structure, implemented in the Python materials genomics (Pymatgen) library.^{89,90}

After screening, we end up with 190 non-duplicate candidates compared to C2DB. This relatively large number of candidates highlights CDVAE’s ability to generate new materials, especially when considering that more than 3000 materials in the database have been added to the database by a CDVAE model. This potentially indicates CDVAE models are capable of generating new materials from unexplored chemical spaces by simply adjusting the training data to include examples that are representative of the desired properties.

Additionally, only four of these materials out of the 1100 materials were generated through optimization for the energy above the convex hull in latent space. All other materials were generated without optimization for any properties in latent space. It may be that letting the diffusion model explore the chemical space without trying to optimize for a property in latent space could allow it to generate more diverse materials. Since materials in the training data have low energies above the convex hull, this property is inherited in the generated crystals. Interestingly, the thousands of materials added to the C2DB database by a CDVAE model were generated without any optimization of energies above the convex hull.

Proceeding with our workflow, we performed IAP symmetry-constrained optimizations of these crystals followed by DFT relaxations and self-consistent calculations. The relaxed structures are then further screened through four different, independent tests to exclude materials that did not relax into two-dimensional structures.⁹¹⁻⁹³ In this step, a structure is considered to be two-dimensional only if all four dimensionality tests have been passed. This reduces down the total number of materials considered in this work to a final count of 173.

After checking C2DB, Materials Project database, JARVIS, and OQMD for the presence of generated materials, 109 were deemed to be unreported as bulk or two-dimensional with 64 known materials found in OQMD. And all the duplicates we found in JARVIS and the

materials project database were also included in OQMD.

The formation energy per atom, E_f , for each structure was computed using the formula: $E_f = \frac{E_{\text{total}} - \sum_i n_i E_i}{N}$, where E_{total} is the total energy of the structure (obtained for DFT), n_i is the number of atoms of element i in the structure, E_i is the energy of element i obtained from the Materials Project database, and N is the total number of atoms in the structure.

In C2DB, the energy above the convex hull is constructed by considering the formation energy of elementary, binary, and ternary bulk crystals in OQMD.^{5,6} Naturally, this limits the number of considered phases and excludes 2D materials from competing phases. To expand the scope of the considered competing phases, we have computed the energy above the convex hull using the formation energies of compounds available in the Materials Project database and C2DB without any restriction on the number of constituent elements. For competing phases in the Materials Project database, only entries computed with GGA functionals and without the inclusion of a Hubbard U parameter were considered to ensure the exclusion of any energetic inconsistencies that may arise from employing different U values. The distribution of E_{hull} of the monolayers generated through this pipeline are shown in Figure 8. Of the generated monolayers, 91 achieved an E_{hull} of 0, while 171 displayed an $E_{\text{hull}} \leq 0.3$ eV/atom. It is worth noting, that only two materials were found to have $E_{\text{hull}} > 0.3$.

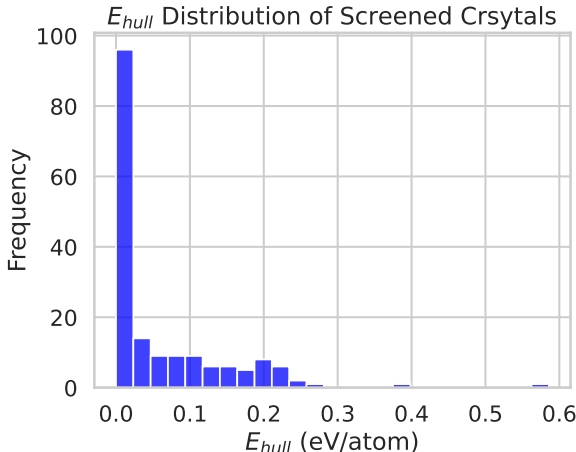


Figure 8: The distribution of E_{hull} of 173 final monolayers generated by the pipeline.

While the energy above the convex hull provides a theoretical assessment of thermo-

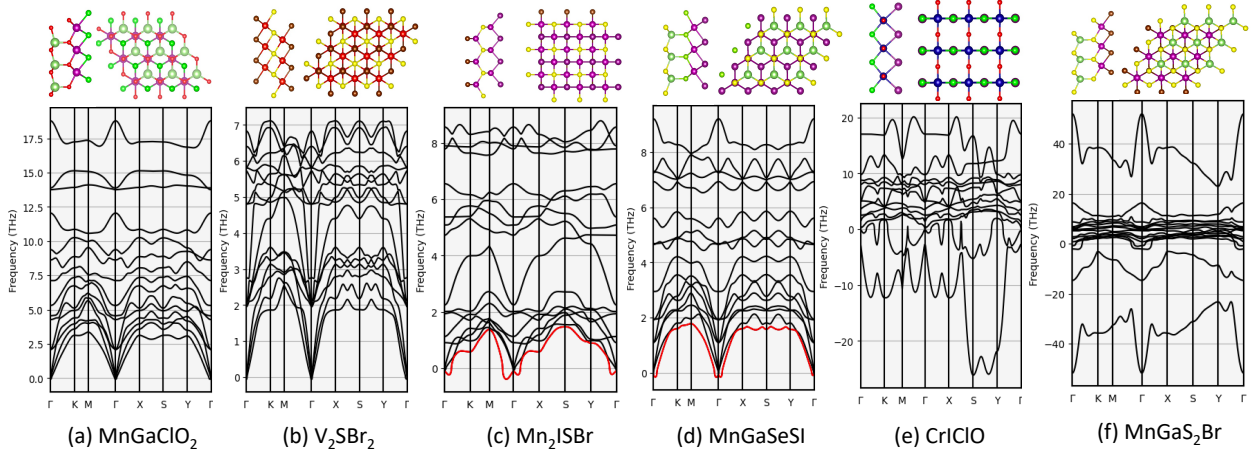


Figure 9: Phonon band dispersions of 6 materials generated through our workflow; (a) and (b) are dynamically stable, (c) and (d) are likely stable, while (e) and (f) are likely unstable. A top and side view of the generated crystals are shown atop each subfigure to the right and left, respectively.

dynamic stability, materials with energies above the convex hull may be experimentally realizable for many reasons. First, PBE functionals deviate from experimental values of formation energies by ≈ 0.25 eV/atom, which in turn affects the accuracy of the energy above the convex hull predictions.⁹⁴ Secondly, the monolayers generated herein are being proposed as freestanding monolayers and ignore external interactions with the environment such as substrate effects that may stabilize these monolayers. For example, silicene has a formation energy of 0.66 eV/atom⁵ but can be synthesized on a metal substrate.^{95,96} Moreover, even materials such as MoS₂ and ZrS₂ with $E_{\text{hull}} > 0$ have been experimentally synthesized.^{5,95} In fact, based on the hull energies of 55 experimentally observed 2D materials, the criterion for high thermodynamical stability of 2D materials was proposed to be $E_{\text{hull}} \leq 0.2$ eV/atom⁵ for calculations performed using PBE functionals. This criterion has been adopted in first-principle calculations to perform a screening of 2D materials suitable for photoelectrocatalytic water splitting.¹²

In addition to thermodynamic stability, mechanical and dynamical stability are also necessary for the realization of 2D materials. Dynamical stability can be assessed through the absence of imaginary modes in the phonon band dispersions of materials. We used the

small-displacements method, implemented in the Phonopy software package,⁹⁷ to calculate the phonon band dispersions of the 6 materials shown in Figure 9. These materials have been confirmed to be magnetic and $E_{\text{hull}} = 0$. Two of these materials, MnGaClO_2 & V_2SBr_2 , display no imaginary phonon modes and therefore are dynamically stable. The phonon band dispersions of Mn_2ISBr & MnGaSeSI show slightly imaginary phonon modes near the Γ point, but are likely dynamically stable. Such slight imaginary modes have been reported in DFT-calculated phonon dispersions of many 2D materials, including experimentally realized ones such as GaSe and have been attributed to interactions between periodic monolayer images and numerical instabilities.^{98–101} These small imaginary modes occur at the long-wavelength limit, typically in the acoustic branch possessing the lowest frequency near the Γ point; we have highlighted this acoustic phonon branch in red for both materials. To the best of our knowledge, these four likely stable crystals have not been reported in bulk or as monolayers in any database at the time of writing.

The last two crystals of MnSeS and CrIClO exhibit large imaginary phonon modes and are likely unstable. Large negative phonon modes typically indicate dynamical instabilities in the structure. However, they may also indicate that the crystal is on the verge of structural transitions or distortions, such as the formation of phases hosting a Charge Density Wave (CDW).¹⁰² For example, MoS_2 undergoes a transition from 1T to 1T' through a 2×1 distorted structure.^{103,104} Furthermore, many transition metal dichalcogenides (TMDs) monolayers undergo a transition to a CDW including NbSe_2 ,¹⁰⁵ TaS_2 ,¹⁰⁶ TaSe_2 ,¹⁰⁷ TiSe_2 ,¹⁰⁸ VS_2 ,¹⁰⁹ and NbTe_2 .¹¹⁰ Moreover, a transition to a CDW has been theoretically predicted for the CrTe_2 monolayer and was shown to stabilize the imaginary phonon modes through crystal by a transition to a $\sqrt{3} \times \sqrt{3}$ supercell.¹¹¹ In fact, because these transitions typically require constructing supercells capable of accommodating the onset of the new phase, one of the approaches to stabilizing such materials is to extend the atoms along the direction of instability. This approach has been utilized as the basis for a high-throughput DFT study to stabilize monolayers that exhibit structural instabilities in C2DB.¹¹ Finally, accounting for

strong electron correlations through a Hubbard U as low as 1 eV has been found to stabilize the imaginary phonon modes in 1T-CrTe₂.¹¹² However, considering the aforementioned approaches to stabilize the materials generated here goes beyond the scope of this work; our aim is to provide motivation and a blueprint for accelerating the discovery and screening of materials with specified properties.

Of the materials analyzed, only two demonstrated a total magnetic moment less than $0.5\mu_B$. On average, materials exhibited a magnetic moment of $4.21\mu_B$. The distribution of the DFT calculated magnetic moments is shown in Figure 10. In subfigure (a), we have binned the total magnetic moments of crystals containing only a single transition metal atom. Clearly, the magnetic moments from the screened structures prominently exhibit peaks at integer values, suggesting a strong correlation with atomic electronic configurations. Notably, while peaks can be observed at the bins representing integer values, any data points are absent at $6\mu_B$ and $7\mu_B$ since configurations with 6 or 7 unpaired electrons are not achievable in a true ground state. As crystals with more magnetic moments are considered (b), we observe an increase of the total magnetization to $\approx 5\mu_B$ and climbing to $\approx 10\mu_B$. Because the considered materials contain at most two transition metal atoms, these large values have likely been produced by two magnetic atoms, each possessing a magnetic moment of $\approx 5\mu_B$.

The pattern largely aligns with the behavior of individual magnetic atoms. This consistency is observed in the majority of the screened structures, where we constrained the number of atoms to five or less, and most compounds featured just one magnetic element. This dataset accentuates the intricate relationship between atomic configurations and resultant magnetic moments, particularly when compounds comprise multiple magnetic atoms.

Overall, from the 190 materials we performed DFT calculations with, 173 were truly two-dimensional. Of those 173, two materials possessed $E_{\text{hull}} > 0.3$ eV/atom and 4 materials displayed a total magnetic moment of less than $0.5\mu_B$. This demonstrates the CDVAE’s capability to generate realistic structures and underscores the efficiency of the discriminator ALIGNN models in learning the underlying distributions of the energy above the convex hull

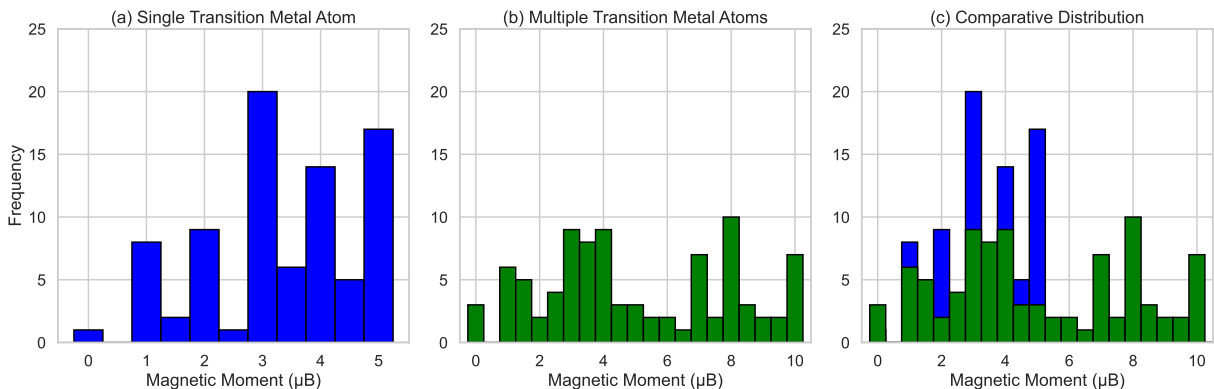


Figure 10: (a) The distribution of the total magnetic moment when a single transition metal atom exists shows peaks at integer values. (b) The distribution of magnetic moments with more than one transient metal atom exhibits a wide range of values. (c) A combined histogram displaying both magnetic moment distributions.

and magnetism.

We have made the monolayer data available at (<https://github.com/rashigeek/2D-mag-GNN>) including the structure of all 173 monolayers. The GitHub repository also includes the code used to produce the results. Additionally, we have provided a complete table of each material, its magnetic moment, and the energy above the convex hull in the supplementary material.

Conclusions

In this study, we presented an integrated computational approach that combines deep learning, symmetry-constrained optimizations, and DFT calculations to generate and screen potential 2D magnetic materials. The process begins with the generation of candidate monolayers using the CDVAE model. Candidates are then rigorously screened based on magnetic probability and thermal stability predictions from trained ALIGNN discriminator models. Screened candidates undergo lattice relaxation using the M3GNet IAP, with final properties computed using DFT.

Our findings demonstrate that the proposed pipeline is effective in predicting magnetic thermodynamically stable monolayers. The observed distributions of magnetic moments

and energies above the convex hull provide a deeper understanding of the interplay between atomic configurations and magnetic properties, revealing distinct patterns and behaviors. By integrating ML and traditional computational techniques, we can expedite the discovery process, paving the way for next-generation materials with properties tailored to specific applications. Moreover, due to the multitude of properties that can also be analyzed using a similar approach to what we have discussed, our work presents a guideline on how to accelerate inverse-design material generation for optimized properties.

Acknowledgement

The authors thank Kristian Sommer Thygesen for kindly providing the C2DB database. Ahmed E. would also like to thank Ryan Paxson for valuable discussions.

This work used EXPANSE at the San Diego Supercomputing Center (SDSC) through allocation PHY220161 from the Advanced Cyberinfrastructure Coordination Ecosystem: Services & Support (ACCESS) program. We acknowledge support from the NSF grant DMR 1709781 and support from the Fisher General Endowment and SET grants from the Jess and Mildred Fisher College of Science and Mathematics at Towson University.

Supporting Information Available

The supplementary information includes a histogram of the number of atoms in magnetic monolayer entries in C2DB, the generated monolayers, their magnetic moments, energies above the convex hull, and their presence in OQMD, MP, C2DB, or JARVIS.

References

- (1) Jain, A.; Ong, S. P.; Hautier, G.; Chen, W.; Richards, W. D.; Dacek, S.; Cholia, S.; Gunter, D.; Skinner, D.; Ceder, G.; Persson, K. A. Commentary: The Materials

- Project: A materials genome approach to accelerating materials innovation. *APL Materials* **2013**, *1*, 011002.
- (2) Choudhary, K.; Garrity, K. F.; Reid, A. C.; DeCost, B.; Biacchi, A. J.; Hight Walker, A. R.; Trautt, Z.; Hattrick-Simpers, J.; Kusne, A. G.; Centrone, A.; others The joint automated repository for various integrated simulations (JARVIS) for data-driven materials design. *npj computational materials* **2020**, *6*, 173.
- (3) Saal, J. E.; Kirklin, S.; Aykol, M.; Meredig, B.; Wolverton, C. Materials Design and Discovery with High-Throughput Density Functional Theory: The Open Quantum Materials Database (OQMD). *JOM* **2013**, *65*, 1501–1509.
- (4) Kirklin, S.; Saal, J. E.; Meredig, B.; Thompson, A.; Doak, J. W.; Aykol, M.; Rühl, S.; Wolverton, C. The Open Quantum Materials Database (OQMD): assessing the accuracy of DFT formation energies. *npj Computational Materials* **2015**, *1*, 15010.
- (5) Hastrup, S.; Strange, M.; Pandey, M.; Deilmann, T.; Schmidt, P. S.; Hinsche, N. F.; Gjerding, M. N.; Torelli, D.; Larsen, P. M.; Riis-Jensen, A. C.; others The Computational 2D Materials Database: high-throughput modeling and discovery of atomically thin crystals. *2D Materials* **2018**, *5*, 042002.
- (6) Gjerding, M. N.; Taghizadeh, A.; Rasmussen, A.; Ali, S.; Bertoldo, F.; Deilmann, T.; Knøsgaard, N. R.; Kruse, M.; Larsen, A. H.; Manti, S.; others Recent progress of the computational 2D materials database (C2DB). *2D Materials* **2021**, *8*, 044002.
- (7) Moustafa, H.; Larsen, P. M.; Gjerding, M. N.; Mortensen, J. J.; Thygesen, K. S.; Jacobsen, K. W. Computational exfoliation of atomically thin one-dimensional materials with application to Majorana bound states. *Physical Review Materials* **2022**, *6*, 064202.
- (8) Butler, K. T.; Davies, D. W.; Cartwright, H.; Isayev, O.; Walsh, A. Machine learning for molecular and materials science. *Nature* **2018**, *559*, 547–555.

- (9) Zuo, Y.; Qin, M.; Chen, C.; Ye, W.; Li, X.; Luo, J.; Ong, S. P. Accelerating materials discovery with Bayesian optimization and graph deep learning. *Materials Today* **2021**, *51*, 126–135.
- (10) Pant, D.; Pokharel, S.; Mandal, S.; Kc, D. B.; Pati, R. DFT-aided machine learning-based discovery of magnetism in Fe-based bimetallic chalcogenides. *Scientific Reports* **2023**, *13*, 3277.
- (11) Manti, S.; Svendsen, M. K.; Knøsgaard, N. R.; Lyngby, P. M.; Thygesen, K. S. Exploring and machine learning structural instabilities in 2D materials. *npj Computational Materials* **2023**, *9*, 33.
- (12) Schleder, G. R.; Acosta, C. M.; Fazzio, A. Exploring two-dimensional materials thermodynamic stability via machine learning. *ACS applied materials & interfaces* **2019**, *12*, 20149–20157.
- (13) Sorkun, M. C.; Astruc, S.; Koelman, J. V. A.; Er, S. An artificial intelligence-aided virtual screening recipe for two-dimensional materials discovery. *npj Computational Materials* **2020**, *6*, 106.
- (14) Wang, H.-C.; Schmidt, J.; Marques, M. A.; Wirtz, L.; Romero, A. H. Symmetry-based computational search for novel binary and ternary 2D materials. *2D Materials* **2023**, *10*, 035007.
- (15) Wines, D.; Choudhary, K.; Biacchi, A. J.; Garrity, K. F.; Tavazza, F. High-throughput DFT-based discovery of next generation two-dimensional (2D) superconductors. *Nano letters* **2023**, *23*, 969–978.
- (16) Mermin, N. D.; Wagner, H. Absence of ferromagnetism or antiferromagnetism in one- or two-dimensional isotropic Heisenberg models. *Physical Review Letters* **1966**, *17*, 1133.

- (17) Lee, J.-U.; Lee, S.; Ryoo, J. H.; Kang, S.; Kim, T. Y.; Kim, P.; Park, C.-H.; Park, J.-G.; Cheong, H. Ising-type magnetic ordering in atomically thin FePS₃. *Nano letters* **2016**, *16*, 7433–7438.
- (18) Huang, B.; Clark, G.; Navarro-Moratalla, E.; Klein, D. R.; Cheng, R.; Seyler, K. L.; Zhong, D.; Schmidgall, E.; McGuire, M. A.; Cobden, D. H.; others Layer-dependent ferromagnetism in a van der Waals crystal down to the monolayer limit. *Nature* **2017**, *546*, 270–273.
- (19) Gong, C.; Li, L.; Li, Z.; Ji, H.; Stern, A.; Xia, Y.; Cao, T.; Bao, W.; Wang, C.; Wang, Y.; others Discovery of intrinsic ferromagnetism in two-dimensional van der Waals crystals. *Nature* **2017**, *546*, 265–269.
- (20) Fei, Z.; Huang, B.; Malinowski, P.; Wang, W.; Song, T.; Sanchez, J.; Yao, W.; Xiao, D.; Zhu, X.; May, A. F.; others Two-dimensional itinerant ferromagnetism in atomically thin Fe₃GeTe₂. *Nature materials* **2018**, *17*, 778–782.
- (21) Zhang, Z.; Shang, J.; Jiang, C.; Rasmita, A.; Gao, W.; Yu, T. Direct photoluminescence probing of ferromagnetism in monolayer two-dimensional CrBr₃. *Nano letters* **2019**, *19*, 3138–3142.
- (22) Kumari, S.; Pradhan, D. K.; Pradhan, N. R.; Rack, P. D. Recent developments on 2D magnetic materials: challenges and opportunities. *Emergent Materials* **2021**, *4*, 827–846.
- (23) Zhao, B.; Ngaloy, R.; Ghosh, S.; Ershadrad, S.; Gupta, R.; Ali, K.; Hoque, A. M.; Karpiak, B.; Khokhriakov, D.; Polley, C.; others A Room-Temperature Spin-Valve with van der Waals Ferromagnet Fe₅GeTe₂/Graphene Heterostructure. *Advanced Materials* **2023**, *35*, 2209113.
- (24) Wu, H.; Zhang, W.; Yang, L.; Wang, J.; Li, J.; Li, L.; Gao, Y.; Zhang, L.; Du, J.;

- Shu, H.; others Strong intrinsic room-temperature ferromagnetism in freestanding non-van der Waals ultrathin 2D crystals. *Nature Communications* **2021**, *12*, 5688.
- (25) Zhao, Z.; Zhou, J.; Liu, L.; Liu, N.; Huang, J.; Zhang, B.; Li, W.; Zeng, Y.; Zhang, T.; Ji, W.; others Two-dimensional room-temperature magnetic nonstoichiometric Fe₇Se₈ nanocrystals: controllable synthesis and magnetic behavior. *Nano Letters* **2022**, *22*, 1242–1250.
- (26) Zhang, G.; Guo, F.; Wu, H.; Wen, X.; Yang, L.; Jin, W.; Zhang, W.; Chang, H. Above-room-temperature strong intrinsic ferromagnetism in 2D van der Waals Fe₃GaTe₂ with large perpendicular magnetic anisotropy. *Nature Communications* **2022**, *13*, 5067.
- (27) Cai, L.; Tung, V.; Wee, A. Room-temperature ferromagnetism in two-dimensional transition metal chalcogenides: Strategies and origin. *Journal of Alloys and Compounds* **2022**, *913*, 165289.
- (28) Zhang, X.; Lu, Q.; Liu, W.; Niu, W.; Sun, J.; Cook, J.; Vaninger, M.; Miceli, P. F.; Singh, D. J.; Lian, S.-W.; others Room-temperature intrinsic ferromagnetism in epitaxial CrTe₂ ultrathin films. *Nature communications* **2021**, *12*, 2492.
- (29) Liu, P.; Zhang, Y.; Li, K.; Li, Y.; Pu, Y. Recent advances in 2D van der Waals magnets: Detection, modulation, and applications. *Iscience* **2023**,
- (30) Lee, Y. H. Is it possible to create magnetic semiconductors that function at room temperature? 2023.
- (31) Ontoso, N.; Safeer, C.; Herling, F.; Ingla-Aynés, J.; Yang, H.; Chi, Z.; Martin-Garcia, B.; Robredo, I.; Vergniory, M. G.; De Juan, F.; others Unconventional Charge-to-Spin Conversion in Graphene/Mo Te₂ van der Waals Heterostructures. *Physical Review Applied* **2023**, *19*, 014053.

- (32) Shaginyan, V. R.; Stephanovich, V.; Msezane, A.; Japaridze, G.; Clark, J.; Amusia, M. Y.; Kirichenko, E. Theoretical and experimental developments in quantum spin liquid in geometrically frustrated magnets: A review. *Journal of Materials Science* **2020**, *55*, 2257–2290.
- (33) Banerjee, A.; Bridges, C.; Yan, J.-Q.; Aczel, A.; Li, L.; Stone, M.; Granroth, G.; Lumsden, M.; Yiu, Y.; Knolle, J.; others Proximate Kitaev quantum spin liquid behaviour in a honeycomb magnet. *Nature materials* **2016**, *15*, 733–740.
- (34) Sachs, B.; Wehling, T.; Novoselov, K.; Lichtenstein, A.; Katsnelson, M. Ferromagnetic two-dimensional crystals: single layers of K_2CuF_4 . *Physical Review B* **2013**, *88*, 201402.
- (35) Han, M.-G.; Garlow, J. A.; Liu, Y.; Zhang, H.; Li, J.; DiMarzio, D.; Knight, M. W.; Petrovic, C.; Jariwala, D.; Zhu, Y. Topological magnetic-spin textures in two-dimensional van der Waals $Cr_2Ge_2Te_6$. *Nano Letters* **2019**, *19*, 7859–7865.
- (36) Khela, M.; Dabrowski, M.; Khan, S.; Keatley, P. S.; Verzhbitskiy, I.; Eda, G.; Hicken, R. J.; Kurebayashi, H.; Santos, E. J. Laser-induced topological spin switching in a 2D van der Waals magnet. *Nature Communications* **2023**, *14*, 1378.
- (37) Zhang, X.; Wang, X.; He, T.; Wang, L.; Yu, W.-W.; Liu, Y.; Liu, G.; Cheng, Z. Magnetic topological materials in two-dimensional: theory, material realization and application prospects. *Science Bulletin* **2023**, *68*, 2639–2657.
- (38) Zhu, Y.; Kong, X.; Rhone, T. D.; Guo, H. Systematic search for two-dimensional ferromagnetic materials. *Physical Review Materials* **2018**, *2*, 081001.
- (39) Wang, Y.; Kajihara, S.; Matsuoka, H.; Saika, B. K.; Yamagami, K.; Takeda, Y.; Wadati, H.; Ishizaka, K.; Iwasa, Y.; Nakano, M. Layer-Number-Independent Two-Dimensional Ferromagnetism in Cr_3Te_4 . *Nano Letters* **2022**, *22*, 9964–9971.

- (40) Torelli, D.; Moustafa, H.; Jacobsen, K. W.; Olsen, T. High-throughput computational screening for two-dimensional magnetic materials based on experimental databases of three-dimensional compounds. *npj Computational Materials* **2020**, *6*, 158.
- (41) Horton, M. K.; Montoya, J. H.; Liu, M.; Persson, K. A. High-throughput prediction of the ground-state collinear magnetic order of inorganic materials using density functional theory. *npj Computational Materials* **2019**, *5*, 64.
- (42) Choudhary, K.; Garrity, K. F.; Jiang, J.; Pachter, R.; Tavazza, F. Computational search for magnetic and non-magnetic 2D topological materials using unified spin-orbit spillage screening. *NPJ Computational Materials* **2020**, *6*, 49.
- (43) Minch, P.; Bhattarai, R.; Rhone, T. D. Data-driven study of magnetic anisotropy in transition metal dichalcogenide monolayers. *Solid State Communications* **2023**, 115248.
- (44) Torelli, D.; Thygesen, K. S.; Olsen, T. High throughput computational screening for 2D ferromagnetic materials: the critical role of anisotropy and local correlations. *2D Materials* **2019**, *6*, 045018.
- (45) Xie, Y.; Tritsaris, G. A.; Granas, O.; Rhone, T. D. Data-driven studies of the magnetic anisotropy of two-dimensional magnetic materials. *The Journal of Physical Chemistry Letters* **2021**, *12*, 12048–12054.
- (46) Rhone, T. D.; Bhattarai, R.; Gavras, H.; Lusch, B.; Salim, M.; Mattheakis, M.; Larson, D. T.; Krockenberger, Y.; Kaxiras, E. Artificial Intelligence Guided Studies of van der Waals Magnets. *Advanced Theory and Simulations* **2023**, 2300019.
- (47) Rhone, T. D.; Chen, W.; Desai, S.; Torrisi, S. B.; Larson, D. T.; Yacoby, A.; Kaxiras, E. Data-driven studies of magnetic two-dimensional materials. *Scientific reports* **2020**, *10*, 15795.

- (48) Bhattarai, R.; Minch, P.; Rhone, T. D. Investigating magnetic van der Waals materials using data-driven approaches. *Journal of Materials Chemistry C* **2023**, *11*, 5601–5610.
- (49) Chen, T.; Guestrin, C. XGBoost: A Scalable Tree Boosting System. Proceedings of the 22nd ACM SIGKDD International Conference on Knowledge Discovery and Data Mining. New York, NY, USA, 2016; p 785–794.
- (50) Acosta, C. M.; Ogoshi, E.; Souza, J. A.; Dalpian, G. M. Machine learning study of the magnetic ordering in 2D materials. *ACS Applied Materials & Interfaces* **2022**, *14*, 9418–9432.
- (51) Zhou, J.; Cui, G.; Hu, S.; Zhang, Z.; Yang, C.; Liu, Z.; Wang, L.; Li, C.; Sun, M. Graph neural networks: A review of methods and applications. *AI Open* **2020**, *1*, 57–81.
- (52) Reiser, P.; Neubert, M.; Eberhard, A.; Torresi, L.; Zhou, C.; Shao, C.; Metni, H.; van Hoesel, C.; Schopmans, H.; Sommer, T.; Friederich, P. Graph neural networks for materials science and chemistry. *Communications Materials* **2022**, *3*, 93.
- (53) Xie, T.; Fu, X.; Ganea, O.-E.; Barzilay, R.; Jaakkola, T. S. Crystal Diffusion Variational Autoencoder for Periodic Material Generation. International Conference on Learning Representations. 2022.
- (54) Choudhary, K.; DeCost, B. Atomistic line graph neural network for improved materials property predictions. *npj Computational Materials* **2021**, *7*, 185.
- (55) Chen, C.; Ong, S. P. A universal graph deep learning interatomic potential for the periodic table. *Nature Computational Science* **2022**, *2*, 718–728.
- (56) Sohl-Dickstein, J.; Weiss, E.; Maheswaranathan, N.; Ganguli, S. Deep unsupervised learning using nonequilibrium thermodynamics. International conference on machine learning. 2015; pp 2256–2265.

- (57) Song, Y.; Ermon, S. Generative modeling by estimating gradients of the data distribution. *Advances in neural information processing systems* **2019**, *32*.
- (58) Han, S.; Lee, J.; Han, S.; Moosavi, S. M.; Kim, J.; Park, C. Design of New Inorganic Crystals with the Desired Composition Using Deep Learning. *Journal of Chemical Information and Modeling* **2023**, *63*, 5755–5763.
- (59) Lyngby, P.; Thygesen, K. S. Data-driven discovery of 2D materials by deep generative models. *npj Computational Materials* **2022**, *8*, 232.
- (60) Moustafa, H.; Lyngby, P. M.; Mortensen, J. J.; Thygesen, K. S.; Jacobsen, K. W. Hundreds of new, stable, one-dimensional materials from a generative machine learning model. *Physical Review Materials* **2023**, *7*, 014007.
- (61) Wines, D.; Xie, T.; Choudhary, K. Inverse Design of Next-Generation Superconductors Using Data-Driven Deep Generative Models. *The Journal of Physical Chemistry Letters* **2023**, *14*, 6630–6638, PMID: 37462366.
- (62) Siriwardane, E. M. D.; Zhao, Y.; Hu, J. Data-driven deep generative design of stable spintronic materials. *CrystEngComm* **2023**, *25*, 6017–6029.
- (63) Kingma, D. P.; Welling, M. Auto-encoding variational bayes. *arXiv preprint arXiv:1312.6114* **2013**,
- (64) Batzner, S.; Musaelian, A.; Sun, L.; Geiger, M.; Mailoa, J. P.; Kornbluth, M.; Molinari, N.; Smidt, T. E.; Kozinsky, B. E(3)-equivariant graph neural networks for data-efficient and accurate interatomic potentials. *Nature Communications* **2022**, *13*, 2453.
- (65) Wines, D.; Gurunathan, R.; Garrity, K. F.; DeCost, B.; Biacchi, A. J.; Tavazza, F.; Choudhary, K. Recent progress in the JARVIS infrastructure for next-generation data-driven materials design. *arXiv preprint arXiv:2305.11842* **2023**,

- (66) Kresse, G.; Furthmüller, J. Efficient iterative schemes for ab initio total-energy calculations using a plane-wave basis set. *Physical review B* **1996**, *54*, 11169.
- (67) Kresse, G.; Joubert, D. From ultrasoft pseudopotentials to the projector augmented-wave method. *Physical review b* **1999**, *59*, 1758.
- (68) Perdew, J. P.; Burke, K.; Ernzerhof, M. Generalized gradient approximation made simple. *Physical review letters* **1996**, *77*, 3865.
- (69) Monkhorst, H. J.; Pack, J. D. Special points for Brillouin-zone integrations. *Physical review B* **1976**, *13*, 5188.
- (70) Anisimov, V. I.; Zaanen, J.; Andersen, O. K. Band theory and Mott insulators: Hubbard U instead of Stoner I. *Physical Review B* **1991**, *44*, 943.
- (71) Ylvisaker, E. R.; Pickett, W. E.; Koepernik, K. Anisotropy and magnetism in the LSDA+ U method. *Physical Review B* **2009**, *79*, 035103.
- (72) Georges, A.; Kotliar, G.; Krauth, W.; Rozenberg, M. J. Dynamical mean-field theory of strongly correlated fermion systems and the limit of infinite dimensions. *Reviews of Modern Physics* **1996**, *68*, 13.
- (73) Foulkes, W.; Mitas, L.; Needs, R.; Rajagopal, G. Quantum Monte Carlo simulations of solids. *Reviews of Modern Physics* **2001**, *73*, 33.
- (74) Karp, J.; Hampel, A.; Millis, A. J. Dependence of DFT+ DMFT results on the construction of the correlated orbitals. *Physical Review B* **2021**, *103*, 195101.
- (75) Zang, J.; Wang, J.; Cano, J.; Georges, A.; Millis, A. J. Dynamical mean-field theory of moiré bilayer transition metal dichalcogenides: phase diagram, resistivity, and quantum criticality. *Physical Review X* **2022**, *12*, 021064.

- (76) Jiang, W.; Liu, Y.; Klein, A.; Wang, Y.; Sun, K.; Chubukov, A. V.; Meng, Z. Y. Monte Carlo study of the pseudogap and superconductivity emerging from quantum magnetic fluctuations. *Nature communications* **2022**, *13*, 2655.
- (77) Wines, D.; Tiihonen, J.; Saritas, K.; Krogel, J. T.; Ataca, C. A Quantum Monte Carlo Study of the Structural, Energetic, and Magnetic Properties of Two-Dimensional H and T Phase VSe₂. *The Journal of Physical Chemistry Letters* **2023**, *14*, 3553–3560.
- (78) Wines, D.; Choudhary, K.; Tavazza, F. Systematic DFT+ U and Quantum Monte Carlo Benchmark of Magnetic Two-Dimensional (2D) CrX₃ (X= I, Br, Cl, F). *The Journal of Physical Chemistry C* **2023**, *127*, 1176–1188.
- (79) Priya, P.; Aluru, N. Accelerated design and discovery of perovskites with high conductivity for energy applications through machine learning. *npj Computational Materials* **2021**, *7*, 90.
- (80) Choubisa, H.; Todorović, P.; Pina, J. M.; Parmar, D. H.; Li, Z.; Voznyy, O.; Tamblin, I.; Sargent, E. H. Interpretable discovery of semiconductors with machine learning. *npj Computational Materials* **2023**, *9*, 117.
- (81) Zhao, Y.; Siriwardane, E. M. D.; Wu, Z.; Fu, N.; Al-Fahdi, M.; Hu, M.; Hu, J. Physics guided deep learning for generative design of crystal materials with symmetry constraints. *npj Computational Materials* **2023**, *9*, 38.
- (82) Carpenter, M.; Salje, E.; Howard, C. J. Magnetoelastic coupling and multiferroic ferroelastic/magnetic phase transitions in the perovskite KMnF₃. *Physical Review B* **2012**, *85*, 224430.
- (83) Webster, L.; Yan, J.-A. Strain-tunable magnetic anisotropy in monolayer CrCl₃, CrBr₃, and CrI₃. *Physical Review B* **2018**, *98*, 144411.

- (84) Hu, T.; Wan, W.; Ge, Y.; Liu, Y. Strain-tunable magnetic order and electronic structure in 2D CrAsS₄. *Journal of Magnetism and Magnetic Materials* **2020**, *497*, 165941.
- (85) Larsen, A. H.; Mortensen, J. J.; Blomqvist, J.; Castelli, I. E.; Christensen, R.; Dulak, M.; Friis, J.; Groves, M. N.; Hammer, B.; Hargus, C.; others The atomic simulation environment—a Python library for working with atoms. *Journal of Physics: Condensed Matter* **2017**, *29*, 273002.
- (86) Alchagirov, A. B.; Perdew, J. P.; Boettger, J. C.; Albers, R.; Fiolhais, C. Reply to “Comment on ‘Energy and pressure versus volume: Equations of state motivated by the stabilized jellium model’”. *Physical Review B* **2003**, *67*, 026103.
- (87) Davies, D. W.; Butler, K. T.; Jackson, A. J.; Morris, A.; Frost, J. M.; Skelton, J. M.; Walsh, A. Computational screening of all stoichiometric inorganic materials. *Chem* **2016**, *1*, 617–627.
- (88) Sholl, D. S.; Steckel, J. A. *Density functional theory: a practical introduction*; John Wiley & Sons, 2022.
- (89) Ong, S. P.; Richards, W. D.; Jain, A.; Hautier, G.; Kocher, M.; Cholia, S.; Gunter, D.; Chevrier, V. L.; Persson, K. A.; Ceder, G. Python Materials Genomics (pymatgen): A robust, open-source python library for materials analysis. *Computational Materials Science* **2013**, *68*, 314–319.
- (90) Cheon, G.; Duerloo, K.-A. N.; Sendek, A. D.; Porter, C.; Chen, Y.; Reed, E. J. Data mining for new two- and one-dimensional weakly bonded solids and lattice-commensurate heterostructures. *Nano letters* **2017**, *17*, 1915–1923.
- (91) Pan, H.; Ganose, A. M.; Horton, M.; Aykol, M.; Persson, K. A.; Zimmermann, N. E.; Jain, A. Benchmarking coordination number prediction algorithms on inorganic crystal structures. *Inorganic chemistry* **2021**, *60*, 1590–1603.

- (92) Gorai, P.; Toberer, E. S.; Stevanović, V. Computational identification of promising thermoelectric materials among known quasi-2D binary compounds. *Journal of Materials Chemistry A* **2016**, *4*, 11110–11116.
- (93) Larsen, P. M.; Pandey, M.; Strange, M.; Jacobsen, K. W. Definition of a scoring parameter to identify low-dimensional materials components. *Physical Review Materials* **2019**, *3*, 034003.
- (94) Pandey, M.; Jacobsen, K. W. Heats of formation of solids with error estimation: The mBEEF functional with and without fitted reference energies. *Physical Review B* **2015**, *91*, 235201.
- (95) Malyi, O. I.; Sopiha, K. V.; Persson, C. Energy, phonon, and dynamic stability criteria of two-dimensional materials. *ACS applied materials & interfaces* **2019**, *11*, 24876–24884.
- (96) Li, G.; Zhang, Y.-Y.; Guo, H.; Huang, L.; Lu, H.; Lin, X.; Wang, Y.-L.; Du, S.; Gao, H.-J. Epitaxial growth and physical properties of 2D materials beyond graphene: From monatomic materials to binary compounds. *Chemical Society Reviews* **2018**, *47*, 6073–6100.
- (97) Togo, A.; Chaput, L.; Tadano, T.; Tanaka, I. Implementation strategies in phonopy and phono3py. *Journal of Physics: Condensed Matter* **2023**,
- (98) Radescu, S.; Machon, D.; Mélinon, P. Origin of dynamical instabilities in some simulated two-dimensional materials: GaSe as a case study. *Physical Review Materials* **2019**, *3*, 074002.
- (99) Ataca, C.; Sahin, H.; Ciraci, S. Stable, single-layer MX₂ transition-metal oxides and dichalcogenides in a honeycomb-like structure. *The Journal of Physical Chemistry C* **2012**, *116*, 8983–8999.

- (100) Zheng, H.; Li, X.-B.; Chen, N.-K.; Xie, S.-Y.; Tian, W. Q.; Chen, Y.; Xia, H.; Zhang, S.; Sun, H.-B. Monolayer II-VI semiconductors: A first-principles prediction. *Physical Review B* **2015**, *92*, 115307.
- (101) Zólyomi, V.; Drummond, N.; Fal'Ko, V. Electrons and phonons in single layers of hexagonal indium chalcogenides from ab initio calculations. *Physical Review B* **2014**, *89*, 205416.
- (102) Gruner, G. *Density waves in solids*; CRC press, 2018.
- (103) Qian, X.; Liu, J.; Fu, L.; Li, J. Quantum spin Hall effect in two-dimensional transition metal dichalcogenides. *Science* **2014**, *346*, 1344–1347.
- (104) Liu, L.; Wu, J.; Wu, L.; Ye, M.; Liu, X.; Wang, Q.; Hou, S.; Lu, P.; Sun, L.; Zheng, J.; others Phase-selective synthesis of 1T MoS₂ monolayers and heterophase bilayers. *Nature materials* **2018**, *17*, 1108–1114.
- (105) Xi, X.; Zhao, L.; Wang, Z.; Berger, H.; Forró, L.; Shan, J.; Mak, K. F. Strongly enhanced charge-density-wave order in monolayer NbSe₂. *Nature nanotechnology* **2015**, *10*, 765–769.
- (106) Yang, Y.; Fang, S.; Fatemi, V.; Ruhman, J.; Navarro-Moratalla, E.; Watanabe, K.; Taniguchi, T.; Kaxiras, E.; Jarillo-Herrero, P. Enhanced superconductivity upon weakening of charge density wave transport in 2 H-TaS₂ in the two-dimensional limit. *Physical Review B* **2018**, *98*, 035203.
- (107) Ryu, H.; Chen, Y.; Kim, H.; Tsai, H.-Z.; Tang, S.; Jiang, J.; Liou, F.; Kahn, S.; Jia, C.; Omrani, A. A.; others Persistent charge-density-wave order in single-layer TaSe₂. *Nano letters* **2018**, *18*, 689–694.
- (108) Sugawara, K.; Nakata, Y.; Shimizu, R.; Han, P.; Hitosugi, T.; Sato, T.; Takahashi, T.

- Unconventional charge-density-wave transition in monolayer 1T-TiSe₂. *ACS nano* **2016**, *10*, 1341–1345.
- (109) Van Efferen, C.; Berges, J.; Hall, J.; Van Loon, E.; Kraus, S.; Schobert, A.; Wekking, T.; Huttmann, F.; Plaar, E.; Rothenbach, N.; others A full gap above the Fermi level: the charge density wave of monolayer VS₂. *Nature Communications* **2021**, *12*, 6837.
- (110) Bai, Y.; Jian, T.; Pan, Z.; Deng, J.; Lin, X.; Zhu, C.; Huo, D.; Cheng, Z.; Liu, Y.; Cui, P.; others Realization of Multiple Charge-Density Waves in NbTe₂ at the Monolayer Limit. *Nano Letters* **2023**, *23*, 2107–2113.
- (111) Otero Fumega, A.; Phillips, J.; Pardo, V. Controlled two-dimensional ferromagnetism in 1T-CrTe₂: the role of charge density wave and strain. *The Journal of Physical Chemistry C* **2020**, *124*, 21047–21053.
- (112) Liu, Y.; Kwon, S.; de Coster, G. J.; Lake, R. K.; Neupane, M. R. Structural, electronic, and magnetic properties of CrTe₂. *Physical Review Materials* **2022**, *6*, 084004.

Supporting Information: Accelerated Data-Driven Discovery and Screening of Two-Dimensional Magnets Using Graph Neural Networks

Ahmed Elrashidy,^{*,†} James Della-Giustina,[‡] and Jia-An Yan[†]

[†]*Department of Physics, Astronomy, and Geosciences, Towson University, 8000 York,
Towson, MD 21252, USA*

[‡]*Department of Mathematics, Towson University, 8000 York, Towson, MD 21252, USA*

E-mail: aalras2@students.towson.edu

Table S1: Generated materials sorted by increasing E_{hull} (energy above hull).

Folder No.	Material	μ (Magnetic Moment)	E_{hull} (Energy Above Hull)	Database
4	Mn ₂ SIBr	10.00	0.00	
5	VFeSe ₂	1.68	0.00	OQMD
11	MnTeS	3.05	0.00	OQMD
15	MnRhS ₂	2.76	0.00	OQMD
18	MnInSeIBr	4.46	0.00	
20	CrNiS ₂	0.89	0.00	OQMD
21	MnGaClO ₂	4.83	0.00	
22	MnSeS	2.80	0.00	OQMD

Folder No.	Material	μ (Magnetic Moment)	E_{hull} (Energy above hull)	Database
24	MnInSe ₂ I	4.99	0.00	
25	MnBrClO	3.00	0.00	OQMD
26	MnCl ₂ O	2.70	0.00	OQMD
31	MnBrCl	5.00	0.00	OQMD
32	MnI ₂ O	3.20	0.00	OQMD
33	CrIClO	2.00	0.00	
36	MnClOF	3.00	0.00	
39	MnGaS ₂ Br	5.00	0.00	
41	MnICl	5.00	0.00	OQMD
44	VNCl ₂	0.03	0.00	OQMD
45	FeSeS	1.66	0.00	OQMD
49	MnGaSeSI	4.92	0.00	
51	NiHSO	0.95	0.00	OQMD
52	GaNiO ₂ F	2.00	0.00	
53	NiHOF	2.00	0.00	OQMD
54	MnCrSCl ₂	8.37	0.00	
55	MnTeSe	2.81	0.00	OQMD
58	MnNiS ₂	2.97	0.00	OQMD
59	MnInS ₂ Br	5.00	0.00	
60	MnVTeSe	1.32	0.00	
61	Fe ₂ SeS	-0.00	0.00	OQMD
62	V ₂ SBr ₂	6.00	0.00	
63	Mn ₂ SBrCl	10.00	0.00	
64	Mn ₂ SiCl	10.00	0.00	
68	MnInSBr	5.00	0.00	

Folder No.	Material	μ (Magnetic Moment)	E_{hull} (Energy above hull)	Database
69	MnSeSCl ₂	3.00	0.00	
71	CoHOF	3.00	0.00	OQMD
75	MnNiSCl ₂	6.67	0.00	
76	FeBr ₂ O	4.12	0.00	OQMD
77	GaFeClO ₂	4.00	0.00	
80	MnCoS ₂	2.27	0.00	OQMD
82	MnVSeS	1.74	0.00	
85	CrFeIClO	6.93	0.00	
87	AlCrS ₂ I	3.98	0.00	
88	MnInSIBr	4.48	0.00	
89	FeNiBr ₂ O	5.81	0.00	
91	VSIBr	1.00	0.00	
92	MnInS ₂ I	4.98	0.00	
93	MnInSeSI	5.00	0.00	
94	MnIClO	3.53	0.00	
95	CrFeSICl	6.97	0.00	
99	Mn ₂ IBrO	9.79	0.00	
100	MnVTeS	3.19	0.00	
102	CrBrClO	2.00	0.00	
103	FeHSO	1.00	0.00	OQMD
104	MnCoSeS	2.30	0.00	
111	VFeS ₂	0.99	0.00	OQMD
114	MnSbO ₃	4.00	0.00	OQMD
116	MnCrS ₂ I	8.00	0.00	
118	MnBr ₂ O	3.00	0.00	OQMD

Folder No.	Material	μ (Magnetic Moment)	E_{hull} (Energy above hull)	Database
120	CrNiSBrCl	4.21	0.00	
122	MnAlS ₂ Cl	5.00	0.00	
124	CoBrCl	3.00	0.00	
125	MnVTeCl ₂	7.88	0.00	
127	MnGaSeICl	4.47	0.00	
128	Ti ₂ SiCl	0.00	0.00	
129	MnGaBrO ₂	3.53	0.00	
131	VHClO	3.00	0.00	OQMD
132	MnClF	5.00	0.00	OQMD
133	MnAlS ₂	3.83	0.00	OQMD
134	Mn ₂ TeSBr	8.12	0.00	
136	MnPdSiCl	3.01	0.00	
137	MnVS ₂	0.97	0.00	OQMD
138	MnBiTeSeI	5.00	0.00	
140	GaNiClO ₂	2.00	0.00	
147	Mn ₂ SeSBr	7.00	0.00	
148	VBrClO	1.00	0.00	OQMD
154	VIBrO	1.00	0.00	
157	MnOF ₂	2.78	0.00	OQMD
158	VHClO ₂	1.00	0.00	
159	ZrMnS ₂ Br	4.00	0.00	
160	Ti ₂ S ₂ Cl ₂	-0.00	0.00	
162	ScMnSBr ₂	4.00	0.00	
163	Mn ₂ SeBrCl	10.00	0.00	
164	NbFeSeS	1.47	0.00	

Folder No.	Material	μ (Magnetic Moment)	E_{hull} (Energy above hull)	Database
172	MnGaTeS ₂	3.80	0.00	
175	MnGaSe ₂ Br	4.84	0.00	
177	MnVSBrcI	7.72	0.00	
178	MnVSBrcI	7.72	0.00	
179	MnInSe ₂ Cl	5.00	0.00	
180	CrSeBr ₂	2.07	0.00	
181	NiF ₄	1.11	0.00	
182	MnInSeBr ₂	4.31	0.00	
168	CrSbSe ₂ Br	3.62	0.00	
149	CrFeS ₂	4.47	0.01	OQMD
47	Cr ₂ SBr ₂	8.00	0.01	
113	MgMnSe ₂ I	4.00	0.01	
35	Ni ₂ Br ₂ O	2.00	0.02	OQMD
65	CrGaTe ₃	3.01	0.02	OQMD
115	MnSeI	3.21	0.02	
155	MnSBrCl	3.02	0.02	
142	GaNiSBr ₂	1.07	0.03	
108	MnGeSeBr ₂	5.00	0.03	
109	MnCrS ₂	3.42	0.03	OQMD
84	CrSIBr	2.22	0.03	
9	MnZnSI ₂	5.00	0.03	
43	MnNiSe ₂	3.21	0.03	OQMD
42	Mn ₂ SeBr ₂	10.00	0.04	
12	Mn ₂ SBr ₂	10.00	0.04	
141	MnSeICl	3.14	0.04	

Folder No.	Material	μ (Magnetic Moment)	E_{hull} (Energy above hull)	Database
97	CrNiSe ₂	2.17	0.04	OQMD
151	CrCoSe ₂	1.03	0.05	OQMD
17	FeTeCl	3.38	0.05	OQMD
46	VNiTe ₂	1.13	0.05	OQMD
183	FeCoSe ₂	3.41	0.05	
169	MnNiSBr ₂	6.92	0.05	
171	Mn ₂ TeSI	8.44	0.06	
83	MnCrTeSI	8.00	0.06	
96	FeTeSe	1.55	0.06	OQMD
29	NiIBr	2.00	0.06	OQMD
176	Mn ₂ Te ₂ Se	7.76	0.06	
38	MnZnS ₂ I	4.07	0.07	
34	MnSCl ₂	3.02	0.07	
185	CrSeI ₂	2.00	0.07	
152	Mn ₂ Te ₃	7.92	0.08	OQMD
112	MnPdBr ₂	5.00	0.08	
67	Fe ₂ TeS	3.48	0.08	
188	Mn ₂ SeICl	9.69	0.08	
48	MnTe ₂ Rh	2.80	0.08	OQMD
98	MnNiTeSe	3.00	0.09	
86	MnFeSeS	4.08	0.09	
57	Mn ₂ Se ₃	7.99	0.10	OQMD
189	CrCuS ₂ I	2.89	0.10	
144	FeCoTeSe	3.51	0.10	
126	Fe ₂ SCL ₂	7.97	0.10	

Folder No.	Material	μ (Magnetic Moment)	E_{hull} (Energy above hull)	Database
56	GaFeTeSeBr	3.67	0.10	
16	MnCoSe ₂	5.26	0.11	OQMD
173	MnTe ₃ Rh	4.20	0.11	
117	Fe ₂ TeSe	5.04	0.11	OQMD
7	MnFeS ₂	4.66	0.12	OQMD
0	MnNiTe ₂	3.17	0.12	OQMD
40	MnFeSe ₂	3.43	0.12	OQMD
110	MnCrTe ₃	7.05	0.13	OQMD
10	VFeTe ₂	0.82	0.13	OQMD
27	MnFeTe ₂	3.96	0.14	OQMD
161	MnCrSe ₂	3.36	0.15	
81	Mn ₂ GeTe ₂	3.70	0.15	OQMD
106	Mn ₂ S ₃	7.87	0.15	OQMD
135	MnFeTe ₂ S	6.75	0.15	OQMD
139	MnGeSeI	4.00	0.16	
79	CrTe ₂ Rh	2.42	0.16	OQMD
2	FeNiTe ₂	1.71	0.17	OQMD
123	MnVSe ₂	4.57	0.18	OQMD
13	Mn ₂ TeS	5.68	0.18	OQMD
167	Fe ₂ GeTe ₂	4.23	0.18	
105	MnInSI	5.00	0.18	
37	MnGeTeI	4.00	0.20	
14	Mn ₂ SeS	9.71	0.20	OQMD
74	Mn ₂ TeSe	8.96	0.20	OQMD
150	MnFeS	7.14	0.20	

Folder No.	Material	μ (Magnetic Moment)	E_{hull} (Energy above hull)	Database
119	MnInTe ₂ S	4.03	0.20	
23	MnGeI ₂	3.00	0.21	
166	VGeTe ₂	3.00	0.21	
187	Mn ₂ SBr	8.79	0.21	
165	MnPS ₂	4.17	0.22	
107	MnGeTeS	3.00	0.22	
121	MnGeI	3.91	0.22	
30	MnGe ₂ ICl	3.88	0.22	
70	MnGeCl	3.51	0.22	
90	MnGeBr	3.82	0.23	
66	FeCoTe ₂	2.70	0.25	OQMD
73	MnCrTe ₂	8.40	0.26	OQMD
146	Mn ₂ TeSe ₂	4.12	0.26	OQMD
143	MnSbTeI	4.37	0.40	
1	MnNiSeI ₂	3.59	0.59	

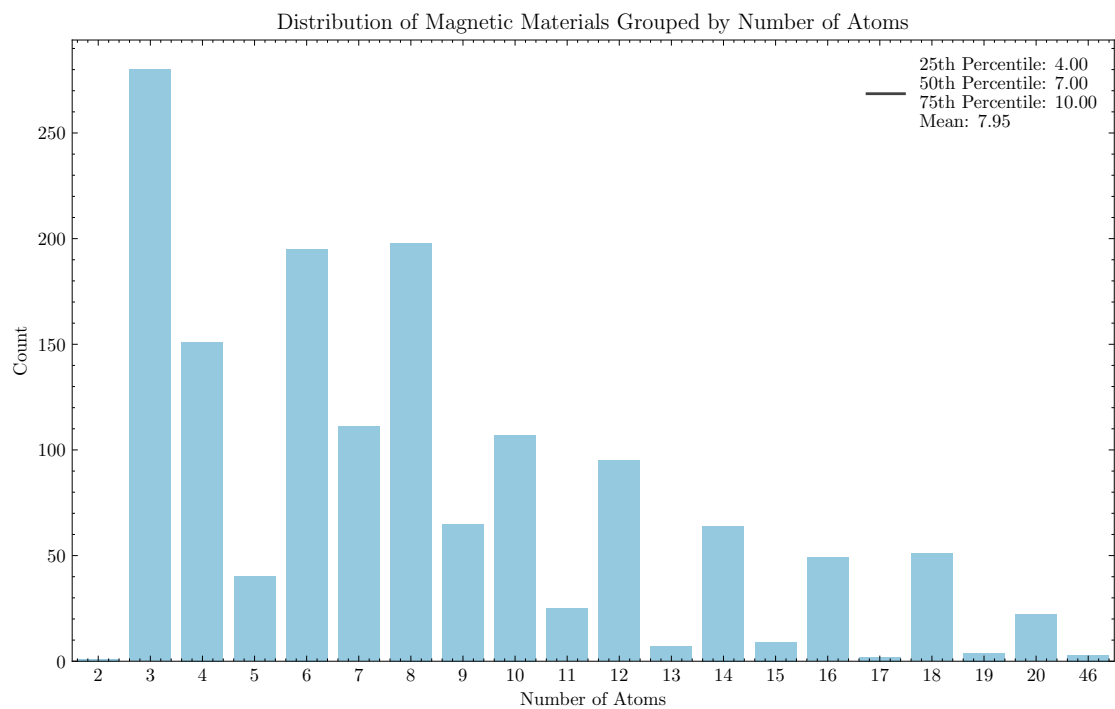


Figure S1: A histogram of the number of atoms in magnetic monolayer entries in C2DB along with percentiles values.

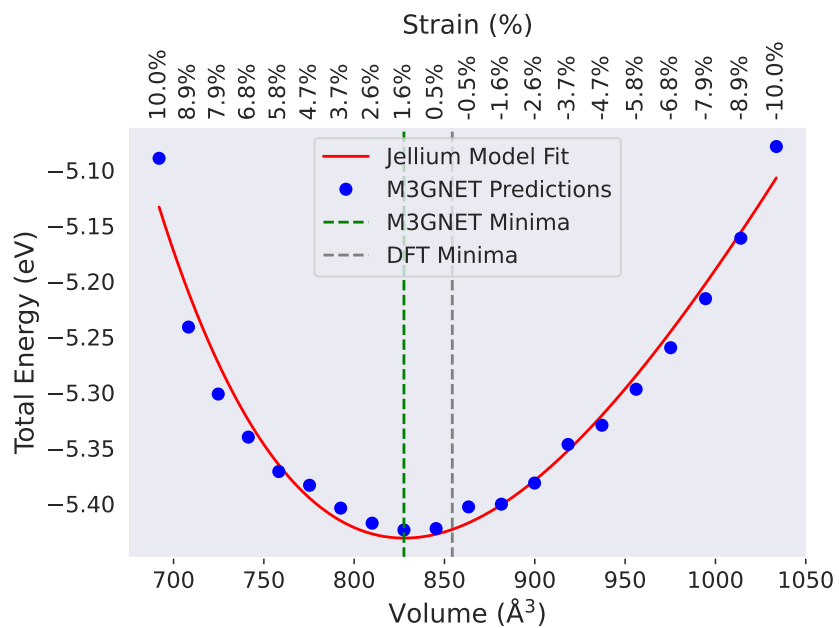


Figure S2: Jellium model fit of the PES generated by ALIGNN-FF